Double-folding analysis of elastic and inelastic ³He-nucleus scattering at 60 MeV

A. F. Hamza^{1†} N. A. El-Nohy^{2‡}

¹Department of Physics and Chemistry, Faculty of Education, Alexandria University, Alexandria, Egypt ²Physics Department, Faculty of Science, Alexandria University, Alexandria, Egypt

Abstract: This study investigated the elastic and inelastic scattering of ³He particles from ¹²C, ¹⁶O, ²⁴Mg, and ²⁸Si nuclei at 60 MeV using a double-folding approach with four newly derived effective nucleon-nucleon (NN) interactions (R3Y(HS), R3Y(L1), R3Y(W), and R3Y(Z)) derived from the relativistic mean-field theory. The four derived effective NN interactions exhibited strong sensitivity to the choice of exchange potential. Regularizing the NN interactions improved the agreement between calculated folded potentials and experimental data. Normalization constants for the R3Y(HS) interaction suggested its superiority over the R3Y(L1) and R3Y(W) interactions within the double-folding framework. Transition potentials based on two models, deformed potential and double folding potential, were used to describe inelastic scattering. Physically consistent deformation parameters were obtained. The deformed potential model yielded better results for ¹²C and ¹⁶O, whereas the double folding model performed better for ²⁴Mg and ²⁸Si, suggesting that the advantage of the double folding model is limited to lighter targets. The Bohr-Mottelson transition density effectively described 2⁺ states; however, it was less suitable for the 3⁻ state of ¹⁶O, for which a Tassie-like transition density provided improved agreement.

Keywords: optical model, double folding model, effective NN interactions, regulation, DWBA, coupled-channel method, transition density, deformation parameters

DOI: 10.1088/1674-1137/ade1cb **CSTR:** 32044.14.ChinesePhysicsC.49114101

I. INTRODUCTION

Understanding nucleus-nucleus interactions remains a fundamental challenge in nuclear physics. All observable scattering quantities can be computed once the optical potential is defined, and consequently, the scattering matrix is determined. For heavy-ion collisions, microscopic models such as the double-folding (DF) method have been among the most successful approaches for calculating optical potentials [1–6]. The DF method relies on two key inputs: (1) nuclear densities of colliding nuclei and (2) effective nucleon-nucleon (NN) interactions between the projectile and target nucleons. Although nuclear densities can be accurately derived from models or electron scattering experiments, developing a realistic, effective NN interaction remains an open problem [7, 8].

Despite extensive theoretical and experimental efforts, the nature of effective NN interactions remains incompletely understood. Recent progress has been made through the relativistic mean-field (RMF) theory, which has yielded new microscopic NN interactions (e.g., R3Y(HS), R3Y(L1), R3Y(W), and Z). The NN interac-

tion obtained through this theory was remarkably related to the inbuilt fundamental parameters of RMF where the HS, L1, W, and Z parameters were extensively validated in literature to reproduce nuclear ground-state properties such as binding energies, charge radii, and deformation parameters [9, 10]. These interactions have been successfully applied to cluster radioactive decays [11, 12] and used for investigating the elastic scattering cross-sections of proton and neutron haglo nuclei [7] and the analysis of $^6\text{Li}(^3\text{He},d)^7\text{Be}$ transfer reactions [13]. However, further validation is required, particularly in intermediate-energy scattering, where nuclear and Coulomb forces play significant roles.

A primary source of knowledge related to the characteristics of ground and low-lying excited states of atomic nuclei is the study of the elastic and inelastic processes of the helium isotope ³He interaction with the nuclei [14]. Over the past few decades, researchers have extensively investigated ³He scattering on light nuclei at energies reaching 150 MeV [15–23]. The energy range of the incident particles can be classified into three major categories. The first category includes energies below 15–20

Received 25 April 2025; Accepted 6 June 2025; Published online 7 June 2025

[†] E-mail: a.hamza@alexu.edu.eg

[‡] E-mail: nazih.elnohy@alexu.edu.eg

^{©2025} Chinese Physical Society and the Institute of High Energy Physics of the Chinese Academy of Sciences and the Institute of Modern Physics of the Chinese Academy of Sciences and IOP Publishing Ltd. All rights, including for text and data mining, AI training, and similar technologies, are reserved.

MeV. In this range, the Coulomb interaction is the dominant scattering determinant, and the inner region of the nucleus does not affect differential cross-sections. In the second category, nuclear forces become relevant with incident particle energies of 20–40 MeV. Consequently, the scattering presents a different characteristic, and a diffraction pattern appears in the angular distributions, similar to that of an absorbing sphere. In the third category, the ³He scattering properties change at energies greater than 40 MeV. Recently, the elastic-scattering data of ³He on ¹²C, ¹⁶O, ²⁴Mg, and ²⁸Si at 60 MeV have been used for experimentally determining the parameters of optical potentials [19, 22, 24, 25].

This work investigates the elastic and inelastic scattering of ³He from ¹²C, ¹⁶O, ²⁴Mg, and ²⁸Si at 60 MeV using a DF model with RMF-derived NN interactions. We aim to evaluate the performance of R3Y(HS), R3Y(L1), R3Y(W), and R3Y(Z) interactions in reproducing elastic scattering data; examine the impact of NN interaction regularization and exchange potentials on cross-section predictions; determine the optimal NN interaction and associated parameters for describing ³He scattering; compare the deformed potential (DP) and DF models for inelastic scattering to excited states; and investigate the sensitivity of inelastic scattering descriptions to the choice of transition potential model and relevance of Bohr-Mottelson and Tassie models for describing collective nuclear excitations. The theoretical framework of this study is presented in Sec. II. The results of the calculations are reported in Sec. III, analyzing scattering observables obtained from the DF model for the various target nuclei and discussing the sensitivity of the results to model parameters and associated uncertainties. Finally, Sec. IV summarizes the key findings, discusses their implications for our understanding of ³He-nucleus scattering, and outlines potential avenues for future research.

II. THEORETICAL FORMALISM

A. Elastic scattering

In the DF approach, the real part of the optical potential is generated by folding the matter density of the projectile and target with an effective NN interaction [26]. The folded potential can be expressed as

$$V^{DF} = V^D + V^{EX}, (1)$$

where V^D and V^{EX} represent the direct and exchange potentials, respectively. The direct part of the folded potential, which represents the nuclear interaction independent of nuclear spins and isospins, takes the form

$$V^{D}(\vec{r}, E) = \int d^{3}\vec{r}_{p} d^{3}\vec{r}_{t} \rho_{p}(\vec{r}_{p}) \rho_{t}(\vec{r}_{t}) v_{NN}^{D}(\vec{s}, E) , \vec{s} = \vec{r} + \vec{r}_{t} - \vec{r}_{p},$$
(2)

where $\rho_{p,t}$ represent the nuclear matter densities of the projectile and target, respectively. v_{NN}^D represents a direct part of the NN effective interaction. The exchange part V^{EX} , which considers the effect of a single knock-on exchange, has two forms. The first form is expressed as [1]

$$V^{EX}(\vec{r}, E) = \int d^3 \vec{r}_p \ d^3 \vec{r}_t \ \rho_p(\vec{r}_p) \ \rho_t(\vec{r}_t) \ \widehat{J}_{00}(E) \delta(\vec{s}), \quad (3)$$

where $\widehat{J}_{00}(E)$ represents the strength of the exchange term, which exhibits a weak linear dependence on energy. The Dirac delta function $\delta(s)$ ensures that the interaction is local, effectively transforming it into a zero-range pseudo-potential. This form is widely used in heavy-ion scattering studies. The knock-on interaction $J_{00}(E)\delta(s)$ is a semi-phenomenological formula that requires calibration for both nucleon-nucleus and nucleus-nucleus scattering.

A more rigorous and theoretically grounded approach for approximating the exchange potential has been proposed as an alternative to the simpler, semi-phenomenological approach of the first form [1]. This approach explicitly accounts for the finite range of the interaction. Although this form is non-local, some studies [27, 28] demonstrated that an accurate local approximation can be obtained by treating the relative motion locally as a plane wave, yielding the expression

$$V^{EX}(\vec{r}, E) = \int d^3 \vec{r}_p d^3 \vec{r}_t \, \rho_p(\vec{r}_p, \vec{r}_p + \vec{s}) \, \rho_t(\vec{r}_t, \vec{r}_t - \vec{s})$$

$$\times v_{\text{NN}}^{EX}(\vec{s}, E) \exp\left(\frac{i\vec{K}(\vec{r}).\vec{s}'}{\mu}\right) , \quad (4)$$

with

$$v_{\text{NN(M3Y-Reid)}}^{EX}(s,E) = \left[4631 \frac{e^{-4s}}{4s} - 1787 \frac{e^{-2.5s}}{2.5s} -7.847 \frac{e^{-0.7072s}}{0.7072s}\right] (1 - 0.002\varepsilon),$$
(5)

$$v_{\text{NN(M3Y-Paris)}}^{EX}(s, E) = \left[-1524.25 \frac{e^{-4s}}{4s} - 518.75 \frac{e^{-2.5s}}{2.5s} -7.8474 \frac{e^{-0.7072s}}{0.7072s} \right] (1 - 0.003\varepsilon),$$
(6)

and

$$\varepsilon = \frac{1}{3} E_{3_{He}},\tag{7}$$

$$K^{2}(r) = \frac{2\mu}{\hbar^{2}} \left[E - V^{DF} - V_{C} \right], \tag{8}$$

where K(r) represents the local momentum of relative motion. This exchange form involves a self-consistency problem, which can be readily solved using a realistic approximation for the density. The potential is then evaluated using an iterative method [26], yielding a local self-consistent potential.

1. Effective NN Interactions

There are several types of effective NN interactions. Such interactions are phenomenological, derived by fitting experimental scattering data and phase shifts. New microscopic NN interactions are derived using the RMF theory. A relativistic mean-field Lagrangian density of a nucleon-meson many-body system is assumed [29–31], and it is constructed from the Lagrangian density of Dirac spinor fields for the nucleons, four different meson fields $(\sigma, \omega, \rho, \text{ and } \delta)$, and the electromagnetic field attributed to the interaction of the charged particles. The solutions of a single NN potential for scalar (σ, δ) and vector (ω, ρ) fields were determined assuming a heavy and static baryonic medium with a one-meson exchange. The resultant effective NN interactions were obtained from the summation of the scalar and vector parts of the single meson fields and defined as [11]

$$v_{\rm NN}(r) = V_{\omega} + V_{\rho} + V_{\sigma} + V_{\delta},\tag{9}$$

$$\nu_{\rm NN}(r) = \frac{g_{\omega}^2}{4\pi} \frac{{\rm e}^{-m_{\omega}r}}{r} + \frac{g_{\rho}^2}{4\pi} \frac{{\rm e}^{-m_{\rho}r}}{r} - \frac{g_{\sigma}^2}{4\pi} \frac{{\rm e}^{-m_{\sigma}r}}{r} - \frac{g_{\delta}^2}{4\pi} \frac{{\rm e}^{-m_{\delta}r}}{r},$$
(10)

where g_{σ} , g_{ω} , g_{ρ} , and g_{δ} represent the coupling constants for σ , ω , ρ , and δ mesons, respectively. m_{σ} , m_{ω} , m_{ρ} , and m_{δ} represent the masses of σ , ω , ρ , and δ mesons, respectively. For a standard nuclear medium, the contribution V_{δ} of δ meson can be neglected compared to the

magnitudes of V_{ω} and V_{σ} . Then, Eq. (10) takes the form

$$\nu_{\rm NN}(r) = \frac{g_{\omega}^2}{4\pi} \frac{e^{-m_{\omega}r}}{r} + \frac{g_{\rho}^2}{4\pi} \frac{e^{-m_{\rho}r}}{r} - \frac{g_{\sigma}^2}{4\pi} \frac{e^{-m_{\sigma}r}}{r}.$$
 (11)

The derived NN interactions from the RMF theory are inserted into Eq. (4) to obtain a real direct folded potential based on RMF. Using the R3Y(HS) parameters from Table 1 in Eq. (11) as illustrative examples, one can obtain ((See left panel of Fig. 1)

$$v_{\text{NN}}^{(HS)}(r) = 11956.94 \frac{e^{-3.968r}}{4r} + 4099.06 \frac{e^{-3.902r}}{4r} - 6882.64 \frac{e^{-2.64r}}{4r}.$$
(12)

An essential aspect of using effective NN potentials in the form of the Yukawa potential is related to their regularization caused by singularities. This regularization eliminates the singularities at |s| = 0, which lack physical significance. Although the singularity can impact the analysis of NN scattering, it does not pose any challenges when calculating the folding integral for generating the nucleon-nucleus or nucleus-nucleus potential. However, certain studies (e.g., [32, 33]) utilized "regularized" M3Y potentials of the NN interaction that did not include this singularity. In this study, we explore this issue further. Such problems can be attributed to the breakdown of the meson theory at extremely short distances because of the extended structure of nucleons [34]. One-boson-exchange potentials are commonly regularized by incorporating several cut-off factors, including monopole, dipole, and exponential cut-off form factors [35]. In this study, the approach reported in a previous study [33] is followed. The regularized Yukawa function ϕ_c is derived from the Fourier transform to configuration space by incorporating a momentum cut-off form factor $F(\overrightarrow{p})$ as

$$\varphi_C(r) = \frac{4\pi}{m} \int \frac{d^3 \vec{p}}{(2\pi)^3} \frac{e^{i\vec{p}.\vec{r}}}{(\vec{p}^2 + m^2)} F(\vec{p}) , \qquad (13)$$

The cut-off form factor is defined as the nucleon form factor $\rho_N(p)$

Table 1. Parameters of effective NN interactions based on Eq. (11) for different RMF models [11].

Set	m_{σ} /MeV	m_{ω} /MeV	m_{ρ} /MeV	g_{σ}	g_{ω}	$g_{ ho}$	g_{ω}^2/π /MeV	$g_{ ho}^{2}/\pi/\mathrm{MeV}$	g_{σ}^2/π /MeV
R3Y(HS)	520	783	770	10.47	13.80	08.08	11956.94	4099.06	6882.64
L1	550	783	-	10.30	12.60	-	9967.88	_	6660.95
W	550	783	-	09.57	11.67	-	8550.74	_	5750.24
Z	551.31	780	763	11.19	13.83	10.89	12008.98	7445.91	7861.80

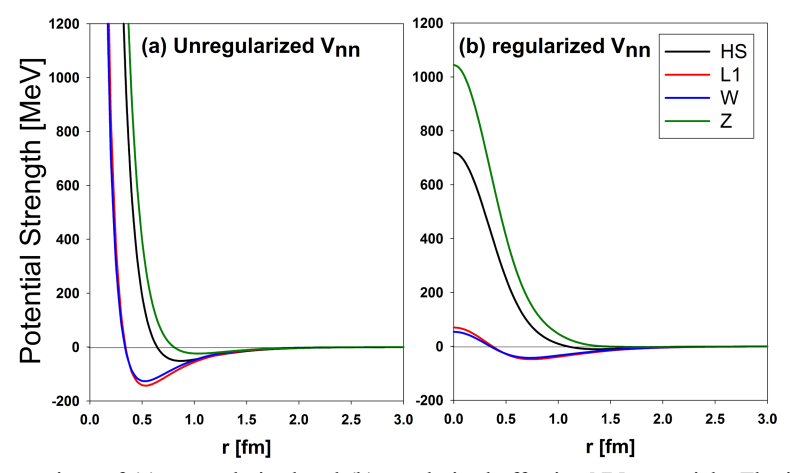


Fig. 1. (color online) Comparison of (a) unregularized and (b) regularized effective NN potentials. The impact of regularization on the shape and strength of the potentials is illustrated.

$$F(\vec{p}) = \int d\vec{r} e^{i\vec{p}.\vec{r}} \rho_N(\vec{p}), \qquad (14)$$

After some transformations, we obtain the following expression for the regularized Yukawa function $\phi_C(r)$ [36]:

$$\varphi_C(r) = \int d\vec{r}_1 \, \rho_N(\vec{r}) \frac{e^{-m||\vec{r} - \vec{r}_1||}}{m \, |\vec{r} - \vec{r}_1|}, \tag{15}$$

Then, the regularized effective NN potential, which consist of three Yukawa functions, can be written in the regularized form as [33]

$$v_{reg}(\vec{r}^{*}) = \int d\vec{r}^{*} \rho_{N}(\vec{r}^{*}) v(\vec{s} = \vec{r}^{*} + \vec{r}^{*})$$

$$= \sum_{i} \frac{g_{i}^{2}}{4\pi} \int d\vec{r}_{1} \rho_{N}(\vec{r}) \frac{e^{-m_{i}|\vec{r} - \vec{r}|}}{|\vec{r} - \vec{r}|} = \sum_{i} \frac{m_{i}g_{i}^{2}}{4\pi} \varphi_{C}^{(i)}(r),$$
(16)

where $\rho_N(\vec{r})$ represents the nucleon density distribution parameterized based on experimental data in [37] using a sum of Gaussian functions:

$$\rho_N(r) = \sum_{i=1}^3 a_i \frac{1}{(\pi r_i^2)^{3/2}} \exp\left(-\frac{r^2}{r_i^2}\right).$$
 (17)

2. Matter Density Distributions

In addition to the effective NN interaction, the folding calculation requires nuclear density distributions for the colliding nuclei. The nuclear matter density distribution of the projectile nucleus ³He is assumed to follow a Gaussian distribution (GD),

$$\rho_M(r) = \rho_M(0) \exp(-\beta r^2), \tag{18}$$

For the target nuclei, the densities are assumed to follow modified Gaussian distributions, which exhibit a nuclear bubble structure [38]; see Fig. 2.

$$\rho_M(r) = \rho_M(0) \left[1 + \omega r^2 \right] \exp(-\beta r^2), \tag{19}$$

where $\rho_M(0)$ values were obtained from the normalization condition

$$4\pi \int \rho(r)r^2 dr = A, \tag{20}$$

The parameters for $\rho_M(0)$, ω , and β used in Eqs. (17) and (18) are listed in Table 2.

An imaginary potential (W) is introduced into the optical potential to accommodate absorption into alternative reaction channels. Since surface absorption is determined to predominate within this energy range, the imaginary potential is modeled as a surface potential. Two forms of the imaginary potential are used. The first form consists of a phenomenological potential obtained from the first derivative of a WS potential,

$$W_D^{ph} = -4a W_o \frac{\mathrm{d}}{\mathrm{d}r} \left(1 - \exp\left(\frac{r - R}{a}\right) \right)^{-1}.$$
 (21)

The second form is formulated based on the first derivative of the obtained folded potential itself and is expressed as

$$W_D^{DF} = -4a N_I \frac{\mathrm{d}V^{DF}(r)}{\mathrm{d}r},\tag{22}$$

where a represents the diffuseness parameter of the fol-

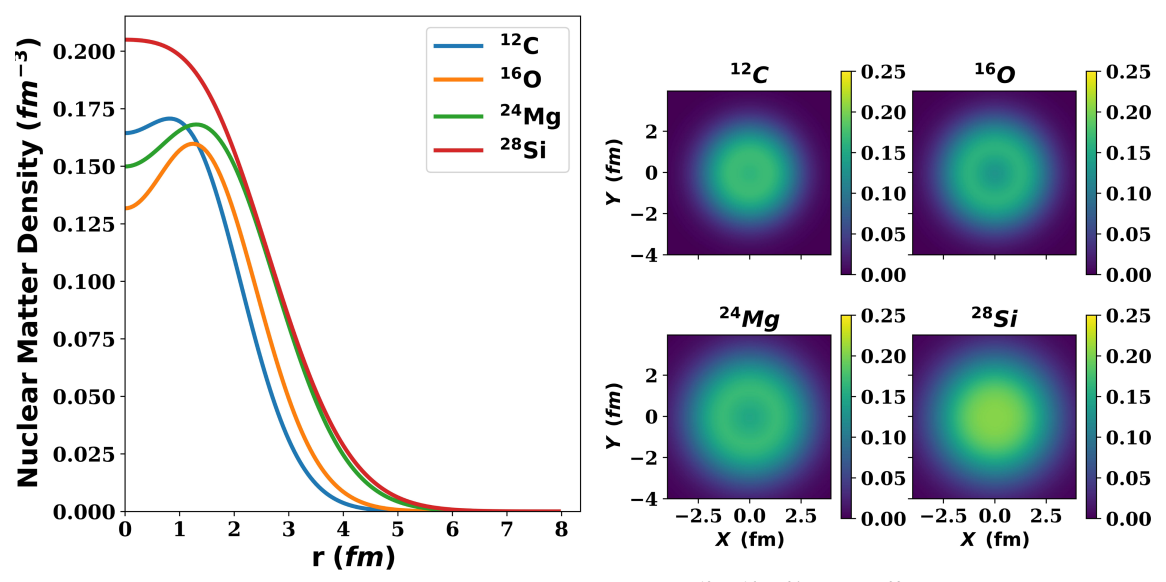


Fig. 2. (color online) Right panel shows the radial nuclear matter densities of ¹²C, ¹⁶O, ²⁴Mg, and ²⁸Si nuclei. The left panel shows 2D nuclear matter distributions.

Table 2. Parameters and root-mean-square (RMS) radii of the nuclear matter densities for ³He [39], ¹²C [40], ¹⁶O [40], ²⁴Mg [41], and ²⁸Si [39].

Nuclei	$ ho_0/\mathrm{fm}^{-3}$	$\omega/{ m fm}^{-2}$	β /fm ⁻²	Calculated RMS radius /fm	Experimental RMS radius /fm
³ He	0.2202	_	0.5505	1.6508	1.976 [42]
¹² C	0.1644	0.4988	0.3741	2.4067	2.46 [43]
$^{16}\mathrm{O}$	0.1317	0.6457	0.3228	2.6401	2.73 [43]
24 Mg	0.1499	0.4012	0.2383	3.0498	3.08 [43]
$^{28}\mathrm{Si}$	0.2052	0.1941	0.2112	3.1378	3.15 [43]

ded potential, obtained by fitting the folded potential to a WS form. N_I represents a normalization constant introduced for scaling purposes. The second form is employed to reduce the number of free parameters and provide a less ambiguous method for examining different effective interactions.

Finally, the local optical potential takes the form

$$U(r,E) = N_R \left[V^D(r,E) + V^{EX}(r,E) \right] + iW(r) + V_C(r), \quad (23)$$

where the real component of the optical potential, denoted as V^{DF} , is scaled by a normalization factor N_R . This normalization factor is incorporated to accommodate minor adjustments required to address dynamic polarization contributions, higher-order effects omitted in the methodology employed to derive the folded potential, and slight uncertainties inherent in the folding inputs. It is anticipated that this factor will remain proximate to unity, affirming the physical significance of the folded potential. The Coulomb potential V_C describing the interaction between the projectile and target is assumed to correspond to the interaction between a point particle and uni-

formly charged sphere with radius R_C . Accordingly, the Coulomb potential is expressed as

$$V_{C}(r) = \begin{cases} \frac{Z_{P}Z_{T}e^{2}}{r} , r \ge R_{C} \\ \frac{Z_{P}Z_{T}e^{2}}{2R_{C}} \left(3 - \frac{r^{2}}{R_{C}^{2}}\right) , r < R_{C}, \end{cases}$$
 (24)

The optical potentials can be characterized by real J_V and imaginary J_W volume integrals per nucleon defined as

$$J_V = -\frac{4\pi}{A_p A_t} \int_0^\infty V(r) r^2 \mathrm{d}r,\tag{25}$$

$$J_W = -\frac{4\pi}{A_p A_t} \int_0^\infty W(r) r^2 \mathrm{d}r. \tag{26}$$

B. Inelastic scattering

For inelastic scattering, the multipole component of

the transition potential U_{λ} is

$$U_{\lambda}(\vec{r}) = V_{\lambda}(\vec{r}) + iW_{\lambda}(\vec{r}) + (V_C)_{\lambda}, \tag{27}$$

In the DF model, the real part of the transition potential of the inelastic scattering is

$$V_{\lambda}(\vec{r}) = N \left[V_{\lambda}^{D}(E, \vec{r}) + V_{\lambda}^{EX}(E, \vec{r}) \right], \tag{28}$$

where $(V_C)_{\lambda}$ represents Coulomb's transition potential, and V_{λ}^D and V_{λ}^{EX} represent direct and exchange transition potentials, respectively. The transition potential is obtained by folding the transition density $\rho_t^{(\lambda)}$, which describes the inelastic excitation of the target nucleus, with the ground-state density of the projectile and effective interaction as [2]

$$V_{\lambda}^{D}(\vec{r}, E) = \int d^{3}\vec{r}_{p} d^{3}\vec{r}_{t} \rho_{p}(\vec{r}_{p}) \rho_{t}^{(\lambda)}(\vec{r}) v_{NN}^{D}(\vec{s}, E), \qquad (29)$$

$$\begin{split} V_{\lambda}^{EX}(\vec{r},E) &= \int \mathrm{d}^{3}\vec{r}_{p} \mathrm{d}^{3}\vec{r}_{t} \, \rho_{p}(\vec{r}_{p},\vec{r}_{p}+\vec{s}) \\ \rho_{t}^{(\lambda)}(\vec{r}_{t},\vec{r}_{t}-\vec{s}) \, v_{\mathrm{NN}}^{EX}(\vec{s},E) \, \mathrm{exp} \left(\frac{\mathrm{i}\vec{K}(\vec{r}).\vec{s}}{\mu} \right). \end{split} \tag{30}$$

A "collective" model is used when the excitation is "isoscalar" and strong [44]. The Bohr–Mottelson (BM) model [45] is adopted in this study. In the BM model, the radial transition density (with $\lambda \ge 2$) is assumed to be proportional to the radial derivative of the ground-state density:

$$\rho_t^{(\lambda)}(r) = -\beta_{\lambda}^m R \frac{\mathrm{d}\rho_t(r)}{\mathrm{d}r},\tag{31}$$

where β_{λ}^{m} and R represent the matter deformation parameter and nucleus radius, respectively; $R = 1.2A^{1/3}$ fm [2].

In the DP model, the radial transition potential is considered proportional to the radial first derivative of the normalized folded potential:

$$V_{\lambda}(r) = -\beta_{\lambda}^{V} R \frac{\mathrm{d}}{\mathrm{d}r} V^{DF}(r), \tag{32}$$

where β_{λ}^{V} represents the deformation parameter of the folded potential $V_{\lambda}(r)$. To compare the DP model with the DF approach for the inelastic form factor, it is assumed that

$$\beta_{\lambda}^{V} = \beta_{\lambda}^{m}. \tag{33}$$

The deformed imaginary part W_{λ} is considered as the deformed surface WS of the phenomenological imaginary elastic scattering potential [46]:

$$W_D(r,\theta) = -4aW_o \frac{\mathrm{d}}{\mathrm{d}r} \left(1 - \exp\left(\frac{r - R(\theta)}{a}\right) \right)^{-1},\tag{34}$$

$$R(\theta) = R_o \left(1 + \beta_{\lambda}^W Y_{\lambda}^0(\theta) \right), \lambda = 2 \text{ or } 3$$
 (35)

Then, W_{λ} has the form [47]

$$W_{\lambda}(r) = \frac{1}{2} \int_{0}^{\pi} W_{D}(r,\theta) P_{\lambda}(\cos(\theta)) \sin(\theta) d\theta.$$
 (36)

The deformation parameter of the imaginary potential serves as a measure of absorption in the considered channel. In this approach, the Coulomb deformation is not included; only the nuclear part of the transition potential is considered. The deformation parameter is adjustable and determined by comparing the computed inelastic cross-section with the observed data. In both models, it is assumed that the real and imaginary deformations are equal,

$$\beta_{\lambda}^{V} = \beta_{\lambda}^{W(DP)}, \beta_{\lambda}^{m} = \beta_{\lambda}^{W(DF)}. \tag{37}$$

Since all deformation parameters are derived by modifying the potentials, they should be denoted as $\beta^{(pot)}$. However, for simplicity, they will be referred to as β . All DF calculations are performed using a modified version of *BiFold* code [48]. The code originally calculates the density-dependent or independent DF potentials between two colliding spherical nuclei. The modifications extend the capability of the code to calculate the transition potentials based on Eqs. (29) and (30).

III. RESULTS AND DISCUSSION

A DF analysis of the ³He elastic and inelastic scattering off ¹²C, ¹⁶O, ²⁴Mg, and ²⁸Si at 60 MeV was performed in this study. The experimental data for elastic and inelastic differential cross-sections were obtained from [19, 22, 24, 25].

A. Elastic scattering

The angular distributions of the elastic and inelastic scattering were calculated using the DF approach. The real part of the optical potential was calculated using new effective NN interactions, and the imaginary part of the optical potential was assumed to have two forms: a surface WS and the first derivative of the folded potential. First, the effective NN interactions were regularized to

consider the effect of regularization on the nucleus-nucleus potential. This study used four effective NN interactions obtained from the RMF model (R3Y(HS), R3Y(L1), R3Y(W), and Z) to examine their validity in describing the elastic and inelastic scattering of light projectiles and investigate their effects on the nucleus-nucleus scattering. Figure 1 illustrates the effective NN interactions before and after regularization. The effect of the cut-off form factor on effective NN interactions removed the singularity. It preserved the potential behavior, which was repulsive at the core and attractive with an increase in separation. The depth of the regularized interactions was reduced to approximately 30% of their original value. At the core, the R3Y(Z) interaction had the largest repulsive strength, followed by the R3Y(HS) interaction and then by the R3Y(L1) and R3Y(W) interactions.

Second, the regularized effective interactions were folded with the nuclear matter densities for ³He and target nuclei. The direct component of folded potentials exhibited a repulsive nature for R3Y(HS) and R3Y(Z) interactions, similar to the DF potentials derived from the M3Y Paris interaction [1]. For R3Y(L1) and R3Y(W) interactions, the direct component of folded potentials was attractive, similar to the DF potentials derived from the M3Y Reid interaction [1]. The exchange part of the folded potential was added to the direct part. The study explored the effects of employing both zero-range and finite-range exchange interactions within the potential

model. Zero-range exchange interactions produced a deeper total folded potential than finite-range exchange interactions, requiring a small normalization constant to fit the differential cross-section data. Therefore, considering the finite-range exchange interactions, the direct potentials were combined with the exchange potential, which resulted in the combination being denoted as R3Y+EX(FR). An additional examination of the exchange potential was conducted with both Reid and Paris finite exchange interactions. For the R3Y(HS) interaction, the direct part R3Y(HS) was combined with both EX(FR/Reid) and EX(FR/Paris) to obtain R3Y(HS)+ EX(FR/Reid) and R3Y(HS)+EX(FR/Paris), respectively. The generated total folded potential based on the Reid interaction was very shallow, making it unsuitable. The obtained shallow potential was similar to that in [7]; the author used Reid EX(ZR), and one can see in Fig. 2 in [7] that the folded potential R3Y(HS)+EX(ZR/Reid) had the smallest depth. Conversely, combining the exchange potential based on the Paris interaction with the direct part of R3Y(HS) produced a more suitable potential than the Reid exchange. For R3Y(L1) and R3Y(W) interactions, the best choice was using the Reid finite exchange potential to generate the total folded potential R3Y(L1)+ EX(ZR/Reid) and R3Y(W)+EX(ZR/Reid). The analysis revealed that the folded potential generated by R3Y(Z)+EX(FR) exhibited a repulsive characteristic, with the majority of the contribution arising from the dir-

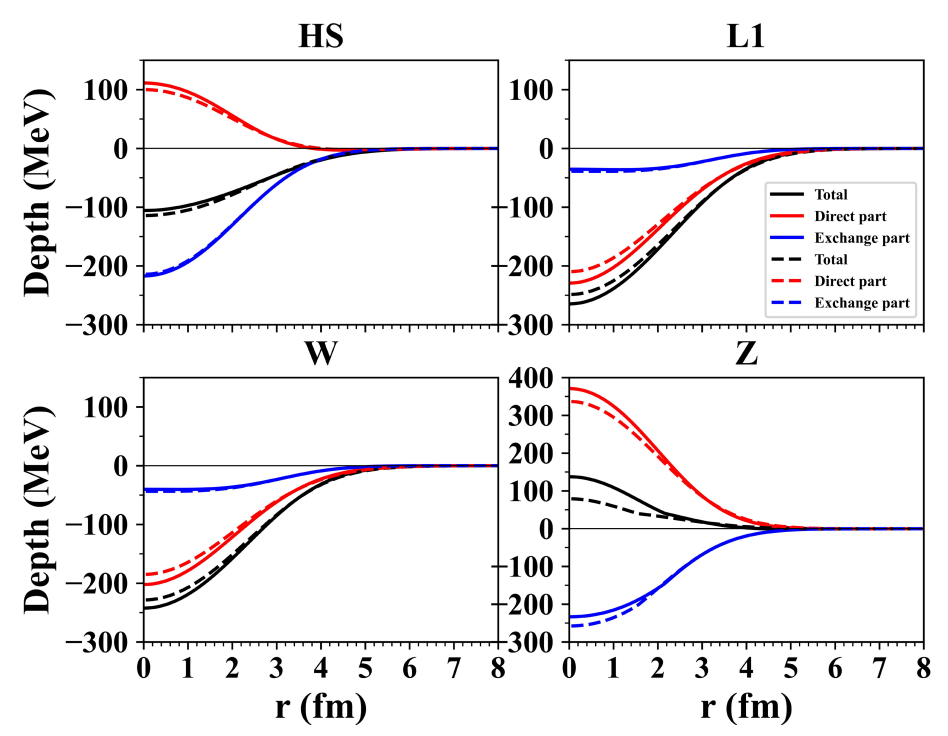


Fig. 3. (color online) Folded potential for ${}^{3}\text{He}{}^{+12}\text{C}$ at 60 MeV based on unregularized (Solid line) and regularized NN effective interactions (Dashed line). The Paris exchange interaction is used for R3Y(HS) and R3Y(Z), whereas the Reid exchange potential is used for R3Y(L1) and W. The colored lines represent the total, direct, and exchange potentials for R3Y+EX(FR).

ect component of the potential (see Fig. 3). Therefore, the R3Y(Z) interaction was excluded from this analysis because a purely repulsive potential for the ³He-nucleus scattering was considered physically meaningless within this energy range. The direct, exchange and total potentials for ¹²C are plotted in Fig. 3.

Folded potentials obtained from regularized effective NN interactions were examined to investigate how regularization affects nucleus-nucleus scattering. The regularization decreased the direct portion of the folded potential while marginally boosting the exchange portion, which resulted in an overall rise in the R3Y(HS) folded potential and decreases in the R3Y(L1) and R3Y(W) folded potentials. The repulsive nature of the folded potential based on the R3Y(Z) interaction remained unchanged by regularization, which reinforced our choice to exclude R3Y(Z) from this analysis. The total folded potentials for ¹²C, ¹⁶O, ²⁴Mg, and ²⁸Si are illustrated in Fig. 4.

Calculations were performed to obtain the elastic scattering cross-sections of the ${}^{3}\text{He}{}^{+12}\text{C}$, ${}^{3}\text{He}{}^{+16}\text{O}$, ${}^{3}\text{He}{}^{+24}\text{Mg}$, and ${}^{3}\text{He}{}^{+28}\text{Si}$ systems at 60 MeV. The folded potentials served as the real component of the optical potentials, whereas surface WS or the derivative of the folded potential was used as the imaginary component. The values of a used to derive the imaginary potentials from the folded potentials based on Eq. (21) and its equivalent WS parameters are listed in Table 3.

Table 4 identifies the optimal parameter set (including normalization and imaginary potential parameters) for describing elastic scattering. The folded potentials derived from regularized interactions effectively fit the experimental data, as shown in Fig. 6. For the ³He+¹²C system, Fig. 5 illustrates how the imaginary component affects the differential cross sections, with the surface Woods-Saxon (SWS) imaginary component outperforming the surface folded derivative (SDF) one. This outcome is expected because the SWS potential incorporates more adjustable parameters such as the depth, radius, and diffuseness of the potential, whereas the SDF potential is restricted to a single parameter N_I that only adjusts the depth of the potential. In addition, a limitation of the SDF potential is its lack of a microscopic foundation and the use of a fixed geometry that may not adequately reflect the absorption process. The assumption that the imaginary part is proportional to the real folded potential part is somewhat arbitrary, and it is employed here merely to simplify the parameter count and facilitate comparisons between different effective interactions. The results in Table 4 show that SWS and SDF potentials provide equivalent normalization constant values across diverse R3Y interactions. Thus, despite its many parameters, the SWS potential may be useful for testing and evaluating R3Y interactions. The choice of imaginary potentials appears to affect the normalization constant, with SDF potentials obtaining slightly higher N_R values than SWS potentials

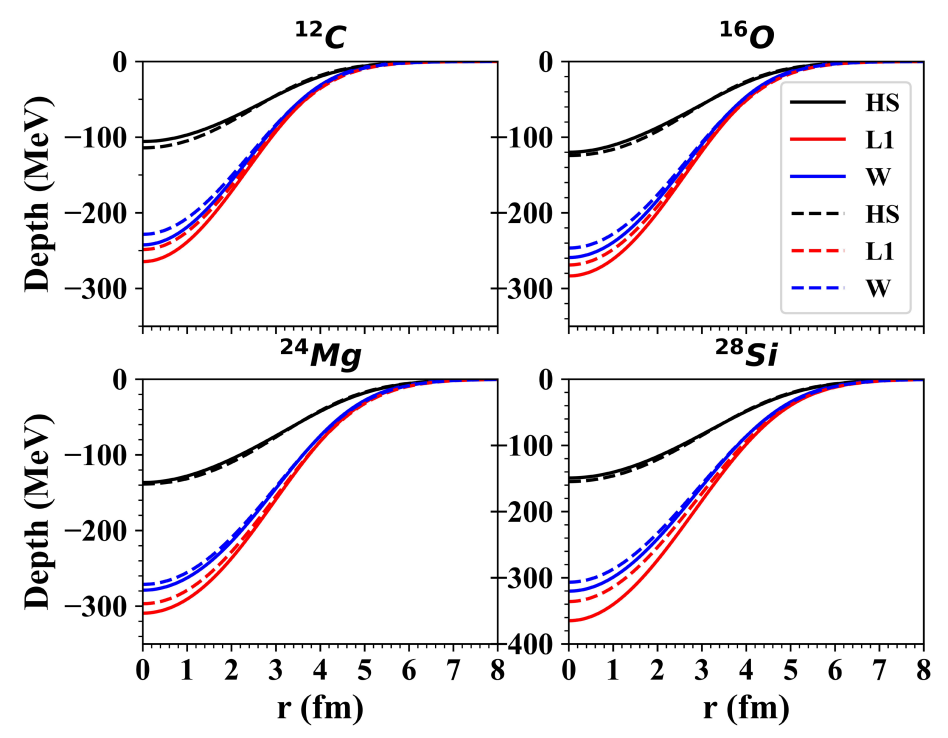


Fig. 4. (color online) Unnormalized folded potentials R3Y(HS)+EX(ZR/Paris) and R3Y(HS)+EX(ZR/Reid) for ³He+¹⁶O, ³He+²⁴Mg, and ³He+²⁸Si at 60 MeV based on unregularized (solid lines) and regularized (dashed lines) effective NN interactions obtained from the RMF model.

Table 3. Parameters of Woods-Saxon potentials equivalent to folded potentials based on the regularized NN interactions R3Y(HS)+ EX(FR/Paris), R3Y(L1)+EX(FR/Reid), and R3Y(W)+EX(FR/Reid).

Reaction	$V_{ m NN}$	V /MeV	R /fm	$a \pm \Delta a$ /fm
	HS	-121.10	2.5412	0.8404±0.0022
$^{3}\text{He}+^{12}\text{C}$	L1	-264.84	2.4338	0.8364 ± 0.0030
	W	-242.97	2.4393	0.8303±0.0029
	HS	-130.51	2.7806	0.8694±0.0023
$^{3}\text{He}^{+^{16}}\text{O}$	L1	-283.92	2.6631	0.8701 ± 0.0032
	W	-259.70	2.6732	0.8632 ± 0.0032
	HS	-144.81	3.1105	0.9453±0.0028
3 He $+^{24}$ Mg	L1	-311.68	2.9864	0.9464 ± 0.0036
	W	-284.34	3.0010	0.9393±0.0035
	HS	-162.70	3.0941	0.9885±0.0032
3 He $+^{28}$ Si	L1	-356.57	2.9348	0.9926 ± 0.0039
	W	-324.94	2.9497	0.9866 ± 0.0038

Table 4. Normalization constants (N_R, N_I) , depth (W_D) , radius and diffuseness parameters $(r_D \text{ and } a_D)$, total cross-sections (σ) , χ^2 values, and volume integrals $(J_R \text{ and } J_I)$ for the theoretical analysis with the regularized NN interactions R3Y(HS)+ EX(FR/Paris), R3Y(L1)+EX(FR/Reid), and R3Y(W)+EX(FR/Reid).

Reaction	V^{DF} + Img.	N_R	J_R /MeV·fm ³	W_D/N_I /MeV	r_D /fm	a_D /fm	J_I /MeV·fm ³	σ_R /mb	χ^2
$^{3}\text{He}+^{12}\text{C}$	R3Y(HS)+SWS	0.98	449.8	19.342	1.298	0.608	164.0	869.3	8.5
	R3Y(HS)+SDF	0.96	441.7	0.13	_	-	157.3	953.9	20.4
	R3Y(L1)+SWS	0.46	414.9	18.480	1.223	0.658	146.2	859.2	4.5
	R3Y(L1)+SDF	0.46	414.9	0.064	-	_	156.4	600.6	14.4
	R3Y(W)+SWS	0.50	413.0	18.378	1.237	0.645	144.6	851.0	5.4
	R3Y(W)+SDF	0.49	411.7	0.070	_	_	155.8	877.4	9.2
³ He+ ¹⁶ O	R3Y(HS)+SWS	0.90	413.6	12.746	1.549	0.686	152.8	1141.3	8.4
	R3Y(HS)+SDF	0.95	436.3	0.14	-	-	165.0	1082.5	22.1
	R3Y(L1)+SWS	0.43	390.8	11.662	1.505	0.769	152.4	1183.0	10.9
	R3Y(L1)+SDF	0.51	460.3	0.079	-	-	188.3	1058.4	31.4
	R3Y(W)+SWS	0.47	386.7	11.488	1.491	0.783	151.1	1185.6	11.4
	R3Y(W)+SDF	0.57	470.6	0.089	-	_	193.0	1059.8	31.5
³ He+ ²⁴ Mg	R3Y(HS)+SWS	0.79	364.8	14.295	1.169	1.067	159.0	1601.1	42.3
	R3Y(HS)+SDF	0.80	367.9	0.14	-	_	163.5	1292.3	53.4
	R3Y(L1)+SWS	0.40	362.6	16.410	1.171	0.980	162.0	1496.2	32.5
	R3Y(L1)+SDF	0.43	387.8	0.075	-	_	176.3	1263.2	71.9
	R3Y(W)+SWS	0.39	318.3	13.513	1.008	1.313	169.2	1848.2	43.1
	R3Y(W)+SDF	0.47	387.8	0.084	_	-	179.6	1262.1	75.15
³ He+ ²⁸ Si	R3Y(HS)+SWS	0.79	357.8	18.243	1.030	1.047	150.9	1571.2	23.8
	R3Y(HS)+SDF	0.82	373.7	0.12	-	_	142.6	1355.0	37.8
	R3Y(L1)+SWS	0.39	349.7	19.723	1.018	0.989	147.3	1473.7	8.6
	R3Y(L1)+SDF	0.40	358.0	0.062	-	-	149.2	1297.6	15.3
	R3Y(W)+SWS	0.43	349.0	19.839	1.021	0.982	147.3	1465.7	9.0
	R3Y(W)+SDF	0.45	368.4	0.070	_	_	153.3	1298.2	16.2

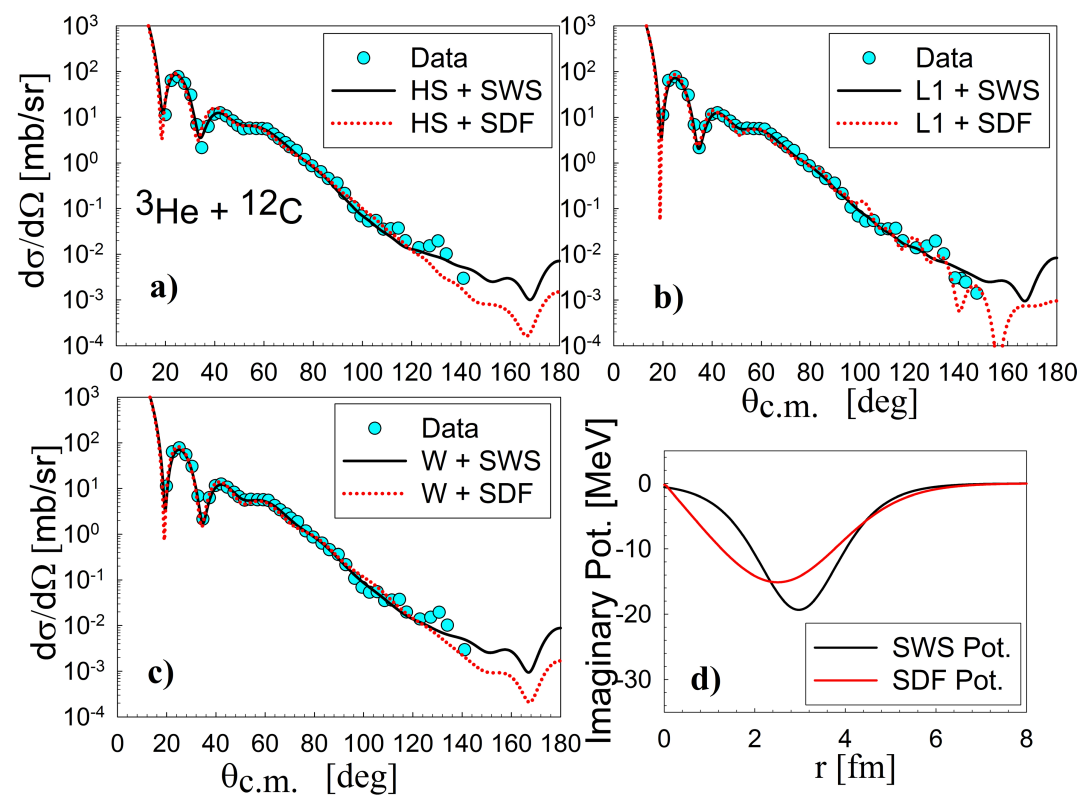


Fig. 5. (color online) Elastic differential cross-sections for ${}^{3}\text{He} + {}^{12}\text{C}$ scattering at 60 MeV calculated with folded potentials using a) R3Y(HS), b) R3Y(L1), and c) R3Y(W) real parts and surface Woods-Saxon (SWS) or folded derivative (SDF) imaginary parts. (d) Comparison of SWS and SDF potentials within the R3Y(HS) model.

but with less fitting (a large χ^2 value). The diffraction pattern at forward angles formed by SDF potentials has a deep first minimum that does not match experimental data, suggesting that the SDF potential may not be the best option. Further, the performance of the SDF potential is highly dependent on the folded potential and its shape; in this scenario, folded potentials obtained from R3Y do not appear to be adequate for generating the imaginary potential at this energy. Moving forward in this study, the SWS potential will be used to simulate the imaginary component of the optical potential in further investigations.

The effect of regularization on elastic differential cross-sections was investigated by comparing calculations using unregularized and regularized NN interactions. Figure 6 demonstrates that regularization consistently enhances differential cross-sections within the diffraction region for all interactions considered. The regularized HS interaction yielded a substantially better fit to the data than the unregularized HS interaction. This improvement suggests that the shape of the folded potentials derived from regularized NN interactions more accurately represents the physical system. The N_R constant associated with the regularized HS interaction was found to be lower than that of the unregularized HS interaction; however, it was higher than those obtained with the un-

regularized L1 and W interactions. Finally, the impact of regularization was negligible for scattering angles less than 25°.

The N_R values for the R3Y(HS) interaction with SWS imaginary potentials are 0.98, 0.90, 0.79, and 0.79 for 12 C, 16 O, 24 Mg, and 28 Si, respectively, with real volume integrals in the range of 350–450 MeV·fm³. The R3Y(L1) and R3Y(W) interactions could reproduce the experimental data with a normalization constant of less than half (see Table 4), indicating that R3Y(L1) and R3Y(W) interactions produced deeper potentials than required. This implies that both interactions are not good candidates for nuclear potentials to describe the 3 He scattering at this energy. N_R decreases with an increase in mass number, which indicates that R3Y interactions are suitable for light nuclei.

B. Inelastic scattering

The inelastic scattering of ³He has been analyzed using the distorted wave born approximation (DWBA) and coupled channels (CC) methods based on the Schrödinger equation for the low-lying 2⁺ state for ¹²C, 3⁻ state for ¹⁶O, 2⁺ state for ²⁴Mg, and 2⁺ state for ²⁸Si at 60 MeV. Two real form factors of the transition potentials were considered: the simple deformed optical potential (DP) and double folded (DF) potential. In the deformed optical po-

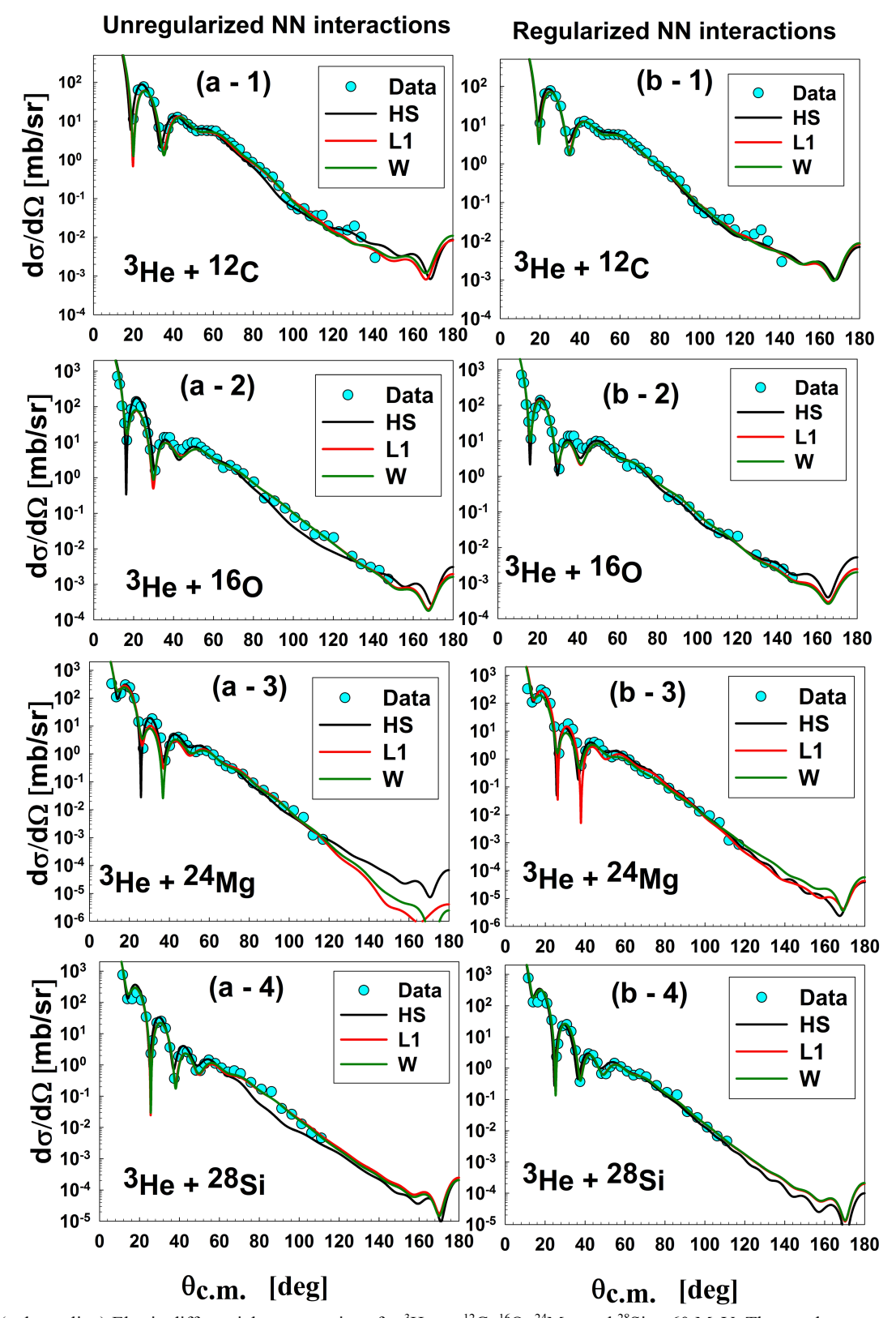


Fig. 6. (color online) Elastic differential cross-sections for ³He on ¹²C, ¹⁶O, ²⁴Mg, and ²⁸Si at 60 MeV. The graphs compare differential cross-sections calculated using a folded potential with different NN interactions: a) unregularized (left) and b) regularized (right). The specific interactions used are R3Y(HS)+EX(FR/Paris), R3Y(L1)+EX(FR/Reid), and R3Y(W)+EX(FR/Reid), all with an SWS imaginary potential.

tential approach, the transition potentials were calculated using Eq. (31). In the folded transition potential approach, the real part of the form factor was calculated by folding the R3Y(HS)+EX(FR/Paris) regularized NN interaction with the ground state of ³He and the target transition density using Eqs. (28) and (29). The R3Y(L1) and R3Y(W) interactions were excluded because of their low normalization constants. The target transition density was assumed to follow the BM model indicated in Eq. (30). The imaginary part of the transition potentials was considered the deformed surface WS potential derived from the semi-microscopic elastic potential as in Eq. (35).

DWBA calculations were carried out using the *ECIS06* code by inserting the real part of the obtained transition potentials and setting the imaginary part parameters. It was assumed that $\beta_R = \beta_I$, and deformation parameters that best fit the inelastic experimental data were searched. The obtained values are listed in Table 5 (see DWBA (DP) and DWBA (DF) columns).

For the low-lying 2⁺ state of ¹²C, the transition potentials based on the DP and DF models, with the R3Y(HS) regularized NN interaction based on the BM model for transition density, are obtained (see Figs. 7(c), 8, and 9(c)). The DP was significantly deeper and possessed a distinct form factor compared to the DF potential. The DP and DF potential described the inelastic scattering well at small angles but failed at large ones (see Fig. 10). This failure confirms the strong coupling between states and supports the application of the CC method. The DP model achieves a better result than the DF model. The deformation parameter obtained from the DP model is consistent with the parameter obtained from the proton scattering, and it is larger than the results obtained from electron and ³He scattering (see Table 5). The deformation parameter obtained from the DF approach has a large value ($\beta = 0.81$). Although this result may indicate that

the DF approach struggles to yield realistic transition potentials, we should not draw this conclusion until we examine the DF approach in the CC framework.

For the low-lying 3⁻ state of ¹⁶O, the DF transition potential did not provide a good fit and required a large deformation parameter. In Fig. 8, the folded potential of the ground state and transition potentials obtained via the microscopic method for multipole $\lambda = 2$ and $\lambda = 3$ are plotted. The depth of the transition potentials decreases with an increase in multipolarity, and therefore, the transition potential for the inelastic 3⁻ state of ¹⁶O requires a large deformation parameter. The ¹⁶O nucleus can exhibit collective excitations in the form of vibrational modes. Although the deep core retains the shape of the ground state in such modes, a few nucleons beyond this core participate in surface oscillations, thereby leading to vibrational spectra [51]. Therefore, it may not be appropriate to treat the transition density of the 3- state in the same way as that of the 2⁺ state. Consequently, it was speculated that the transition density might be the source of the problem. The BM transition density is not suitable for weaker transitions or larger multipolarities [44]. An appropriate deformation parameter can be obtained when a Tassielike (T) transition density [52] is used, wherein the radial transition density is considered.

$$\rho_t^{(\lambda)}(r) = -\tau_{\lambda}^m R \, r \frac{\mathrm{d}\rho_t(r)}{\mathrm{d}r},\tag{38}$$

where τ_{λ}^{m} represents matter deformation with dimensionality (fm⁻¹), which is used to construct the nuclear transition density for a multipole λ .

The transition potential obtained by the Tassie-like transition density denoted as DF-T reproduced the inelastic data better than the transition potential obtained by the BM model, which is denoted as DF-BM (see Fig. 9).

T4	λ^{π}	E 0.637	D ' C I'	Semi-Microscopic					
Target		E_{ex} /MeV	Previous Studies	DWBA (DP)	DWBA (DF)	CC (DP)	CC (DF)		
¹² C	2+	4.44	+0.51 (³ He, ³ He')[49] +0.6 (p, p')[49] ^a -0.45 (e, e')[49]	+0.618	+0.810 (BM) +0.336 (T)	+0.54	+0.719 (BM) +0.313 (T)		
¹⁶ O	3-	6.13	+0.331 (³ He, ³ He') [19]	+0.329	+0.507 (BM) +0.245 (T)	+0.314	+0.511 (BM) +0.249 (T)		
²⁴ Mg	2+	1.37	+0.67 (³ He, ³ He') [24] +0.47 (<i>p</i> , <i>p</i> ') [50] +0.45 (<i>e</i> , <i>e</i> ') [50]	+0.520	+0.655 (BM)	+0.436	+0.562 (BM)		
²⁸ Si	2+	1.78	+0.49 (3He, 3He') [25] -0.37 (p, p') [50] -0.39 (e, e') [50]	+0.386	+0.495 (BM)	+0.322	+0.407 (BM)		

Table 5. Target nuclei, excited state (λ^{π}) , excitation energy $(E_{ex} \text{ in MeV})$, and deformation parameters.

^a The reference did not determine the sign of the parameter

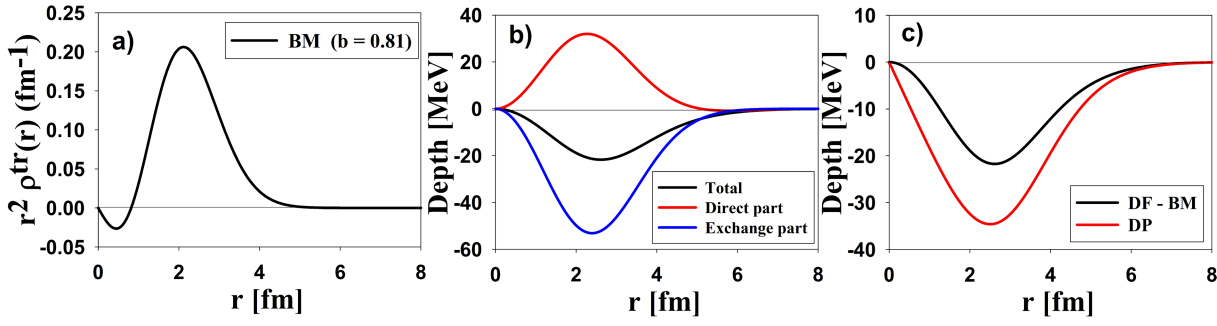


Fig. 7. (color online) a) Transition density for 12 C based on the BM model ($\beta = 0.81$). b) Unnormalized direct and exchange parts of the transition potential based on the DF approach with regularized R3Y(HS)+EX(FR/Paris). c) Transition potentials based on the DP and DF models (setting $\beta R = 1$ for comparison).

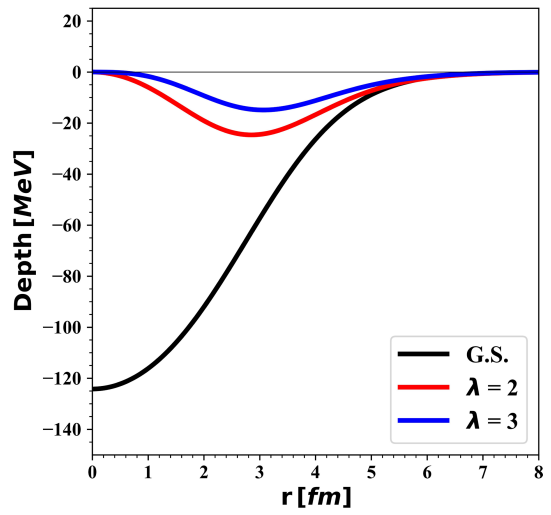


Fig. 8. (color online) Unnormalized ground state folded potential (black line) and transition potentials of ^{16}O for different multipolarities based on the DF approach with R3Y(HS)+EX(FR/Paris) interactions (colored lines) and the BM model for transition density (Setting $\beta_{\lambda}^{m}R = 1$ for comparison).

The deformation parameter obtained from fitting the data has a reasonable value ($\tau = 0.245 \text{ fm}^{-1}$). In Fig. 9, a comparison is made between transition potentials obtained from the BM and T models and the transition potential of

the DP model for the ³He+¹⁶O system. The BM model generated a shallow transition potential, whereas the T model generated the deepest one. Similar to the ¹²C case, both DP and DF models achieve satisfactory results at small angles but fail at large angles. An attempt was made to extend the T model to ¹²C inelastic scattering; however, no satisfactory result was obtained. The value of the deformation parameter was very small ($\beta = 0.336$) compared to that for the BM model ($\beta = 0.81$). The analysis revealed that the BM model yielded larger deformation parameter values than the T model, particularly when considering the transition potential estimated for 12C and ¹⁶O. A possible explanation for the failure of the Tassie model in describing the 2⁺ state of ¹²C is that this state exhibits rotational rather than vibrational characteristics. The BM collective model, which successfully describes rotational bands, would therefore be more appropriate for ¹²C, in contrast to the Tassie model employed for vibrational excitations [53]. This discrepancy clarifies why the Tassie model effectively represents the vibrational excitations of ¹⁶O; however, the rotating characteristics of ¹²C require the BM model.

The transition potentials of the inelastic 2⁺ state for ²⁴Mg and ²⁸Si were determined for the DP and DF models using BM transition density. Both models yielded satisfactory results for small and large angles. The DP model exhibited a slightly enhanced result, particularly at

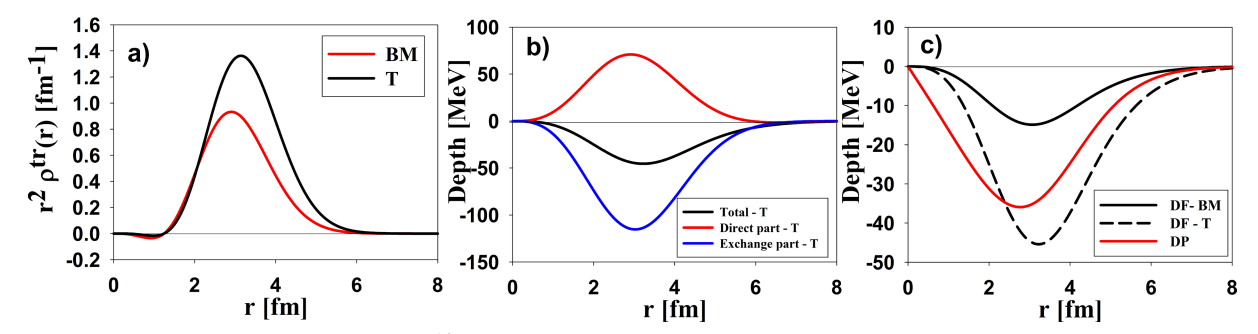


Fig. 9. (color online) a) Transition density of 16 O based on the BM and Tassie-like (T) models (setting $\beta R = \tau R = 1$ for comparison). b) Unnormalized direct and exchange parts of the transition potential are based on the DF calculation for the T model. c) Transition potentials are based on the DP and DF models.

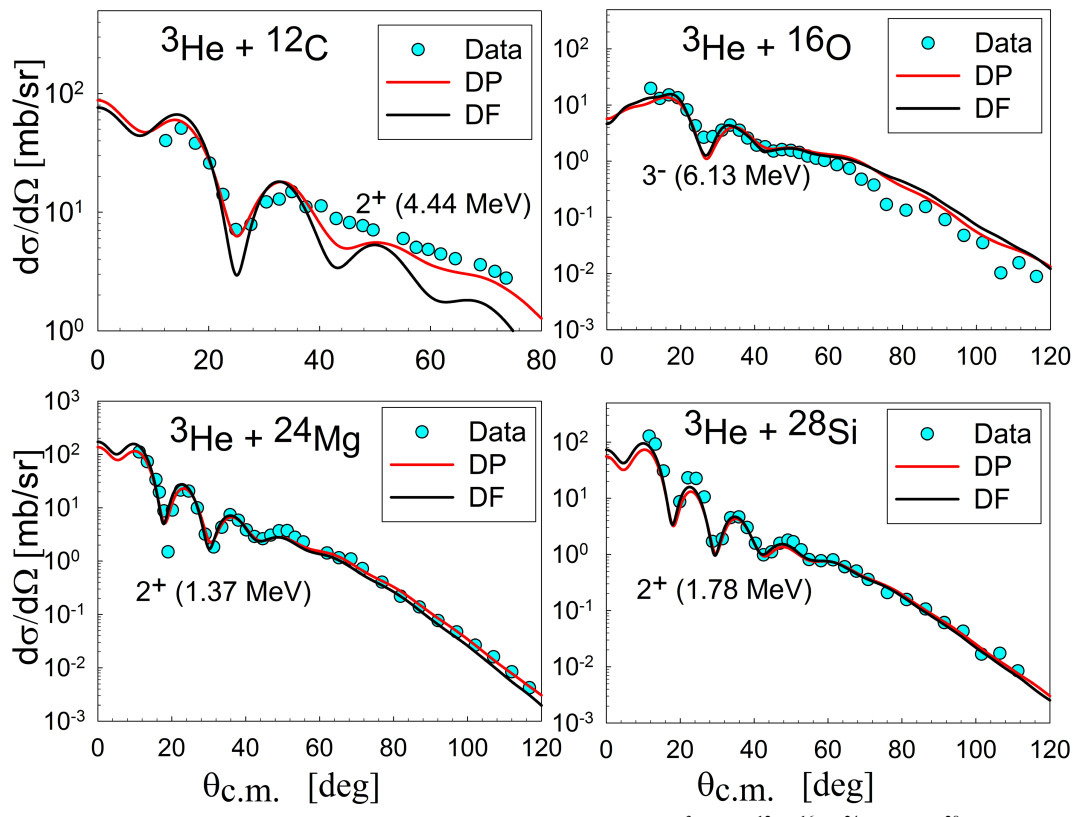


Fig. 10. (color online) DWBA calculations for the elastic scattering of ³He on ¹²C, ¹⁶O, ²⁴Mg, and ²⁸Si at 60 MeV.

large angles. The deformation parameters based on the DF approach are consistent with previous ³He scattering studies ($\beta = 0.655$ and 0.495 for ²⁴Mg and ²⁸Si, respectively). The DP and DF models yield deformation parameters that exceed those derived from electron and proton scattering. The real and imaginary parts of the transition potentials after fitting with the inelastic data were plotted in Fig. 11. The maximum depth for the transition potential of ¹²C, ²⁴Mg, and ²⁸Si ranged between 11 and 14 MeV, whereas for ¹⁶O, the maximum depth was approximately 9 MeV. The root mean square (RMS) radii for the real part of the transition potential were 3.872, 3.865, 4.636, and 4.720 fm for ¹²C, ¹⁶O, ²⁴Mg, and ²⁸Si, respectively. The RMS radii of the transition potential for the 2⁺ state were factors of 1.134, 1.177, and 1.177 larger than the RMS radius for the ground state DF potential of ¹²C, ²⁴Mg, and ²⁸Si, respectively. For the ¹⁶O nucleus, the RMS radius of the transition potential for the 3⁻ state was 1.075 times larger than that of the ground-state DF potential. The calculated RMS radii do not represent the radii of the excited states; instead, they should be interpreted as the RMS radii of the interaction range between the ³He particle and target nuclei. Changes in these radii relative to the ground state can provide insights into nuclear deformation. These changes for ¹²C, ²⁴Mg, and ²⁸Si exceed that of ¹⁶O, likely because of their significant static nuclear deformation.

Next, the CC method was applied to measure the

strength of coupling between states based on the semi-microscopic optical potentials. In the CC calculations, the (0⁺, 2⁺) coupling schemes were studied using the collective rotational model for ¹²C, ²⁴Mg, and ²⁸Si, whereas the (0⁺, 3⁻) coupling schemes were used for ¹⁶O. The CC calculations involved the variation of the normalization constant, surface WS potential parameters, and deformation parameters permitted to simultaneously optimize the fit for elastic and inelastic data. The results are listed in Table 6. The deformation parameters are listed in Table 5 (see CC (DP) and CC (DF) columns). Potentials derived from elastic scattering were utilized as initial potentials for CC calculations, with inelastic data incorporated into the process. Channel coupling was found to affect the ground-state scattering behavior [54, 55], which requires a comparison of CC calculations for both elastic and inelastic cross-sections.

First, the coupling effect on the elastic scattering was analyzed. The sensitivity of the coupling to the inelastic form factor was explored by examining the DP and DF models. The elastic scattering with and without coupling was depicted in Fig. 12 for both models. The CC method accurately described elastic scattering within the angular range of 10 to 100°. For the ¹²C nucleus, the CC approach produced an oscillation within the angular range of 80 to 120°, which was consistent with the data and not observed in the DWBA method. The CC calculation based on the DP, referred to as CC-DP, had a better res-

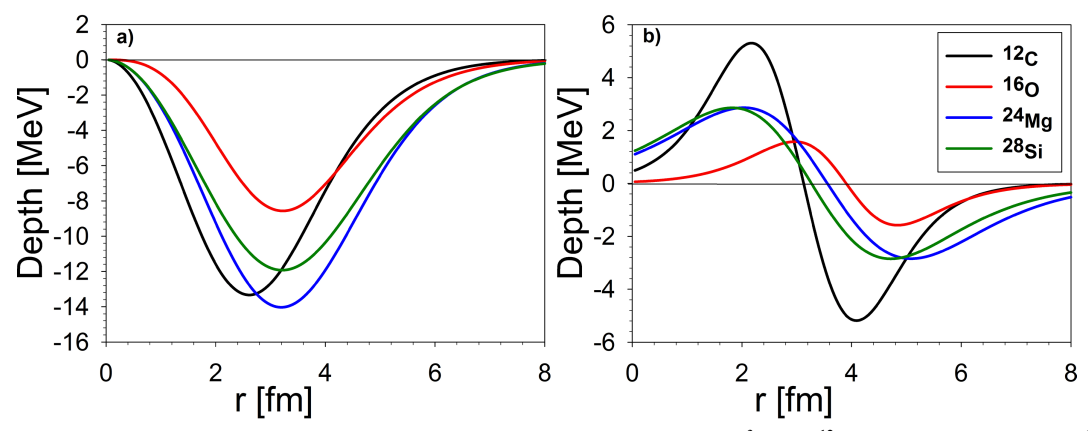


Fig. 11. (color online) a) Real part of the DF transition potentials for the scattering of ³He on ¹²C (⁺2 state – BM model), ¹⁶O (⁻3 state – T model), ²⁴Mg (⁺2 state – BM model), and ²⁸Si (⁺2 state – BM model) at 60 MeV based on the regularized HS+EX (FR/Paris) interaction. b) Imaginary part of the transition potentials.

Table 6. Normalization constant (N_R) , depth (W_D) in MeV, radius and diffuseness parameters $(r_D \text{ and } a_D)$, total cross-sections (σ_R) , and χ^2 values of elastic and inelastic scattering for CC calculations based on the folding model with regularized R3Y(HS) interaction.

Reaction	Model	N	W_D /MeV	r_D /fm	a_D /fm	σ_R /mb	β/τ	$\chi^2_{ m elastic}$	$\chi^2_{\rm inelastic}$
3 He $+^{12}$ C	DP	0.863	10.431	1.569	0.596	915.5	+0.54	18.37	2.66
	DF - BM	0.892	10.843	1.569	0.611	915.5	+0.719	30.70	11.2
$^{3}\text{He}^{+16}\text{O}$	DP	0.892	10.969	1.594	0.701	1159.7	+0.314	7.89	151.22
	DF – T	0.861	13.593	0.858	1.126	1249.5	+0.249	9.98	769.91
3 He $+^{24}$ Mg	DP	0.722	9.882	1.230	1.146	1639.3	+0.436	37.3	9.26
	DF - BM	0.739	10.095	1.243	1.126	1624.8	+0.562	37.5	6.52
3 He $+^{28}$ Si	DP	0.761	13.576	1.126	1.037	1546.9	+0.322	12.4	13.1
	DF - BM	0.777	14.055	1.123	1.022	1529.7	+0.407	11.2	11.2

ult than the calculation based on the DF potential, denoted CC-DF, with BM densities. The oscillation was out of phase at angles over 120° in the DF calculation. For the ¹⁶O nucleus, the CC method agreed with the DWBA method up to an angle of 120°. The CC-DF disagreed with both DWBA and CC-DP from a large angle. The effect of coupling was not evident in the ¹⁶O case. No significant difference was observed for the ²⁴Mg and ²⁸Si nuclei compared to the DWBA calculations. The DP results were slightly better than the DF results, except for the ¹⁶O nucleus. The coupling effect consistently decreased the normalization constant across all cases. In addition, the explicit inclusion of inelastic states reduced the depth of the imaginary potentials and required larger values for the radius parameter. In all cases, $r_D > a_D$ is satisfied, except for the DF calculation of ¹⁶O. The CC method yielded larger total reaction cross-sections than the DWBA method.

Second, inelastic cross sections calculated using the CC method were analyzed and presented in Fig. 13. Solid lines depict the results obtained using the DWBA method, whereas dashed lines represent those from the CC method. The CC calculations were initiated with the

most suitable DF transition potentials identified within the DWBA analysis. For the DF model, transition potentials based on the BM model were applied to ¹²C, ²⁴Mg, and ²⁸Si, whereas the T model was utilized for ¹⁶O. For ¹²C, the CC method enhanced the accuracy of results at both small and large angles for both DP and DF potentials (see Fig. 13). This improvement suggested strong coupling between nuclear states. The DP provided a better fit for experimental data than the DF potential. Coupling reduced the deformation parameter by 12.6% for the DP and 11.2% for the DF potential. An evaluation of the DF potential based on the T model showed unsatisfactory results; the small value obtained for the deformation parameters supported the conclusion that the BM transition density was the optimal choice for the 2⁺ state ¹²C.

For the 3⁻ state of ¹⁶O, the CC method provided accurate descriptions within an angular range of 10° to 50°. However, for larger angles, neither CC-DP nor CC-DF showed significant improvement. The calculated cross-sections at angles greater than 80° are significantly higher than the experimental ones. The DWBA results outperformed those of the CC method. This finding aligned

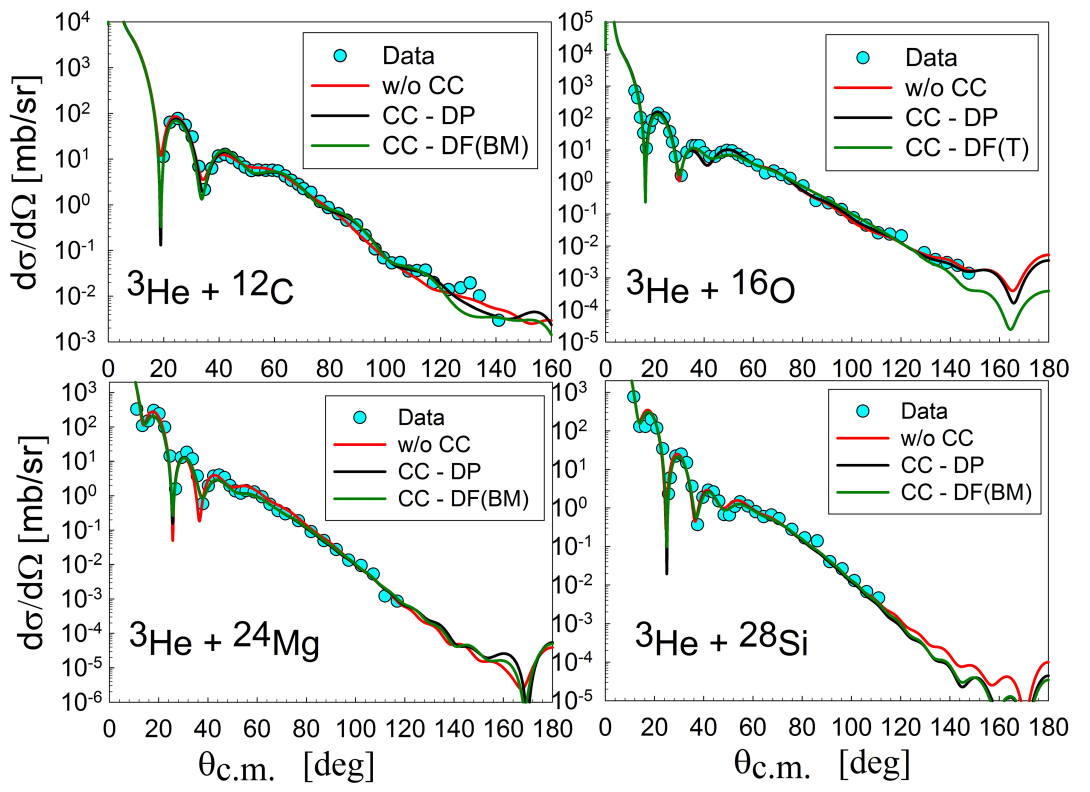


Fig. 12. (color online) Coupled channels calculations for the elastic scattering of ³He on ¹²C, ¹⁶O, ²⁴Mg, and ²⁸Si at 60 MeV.

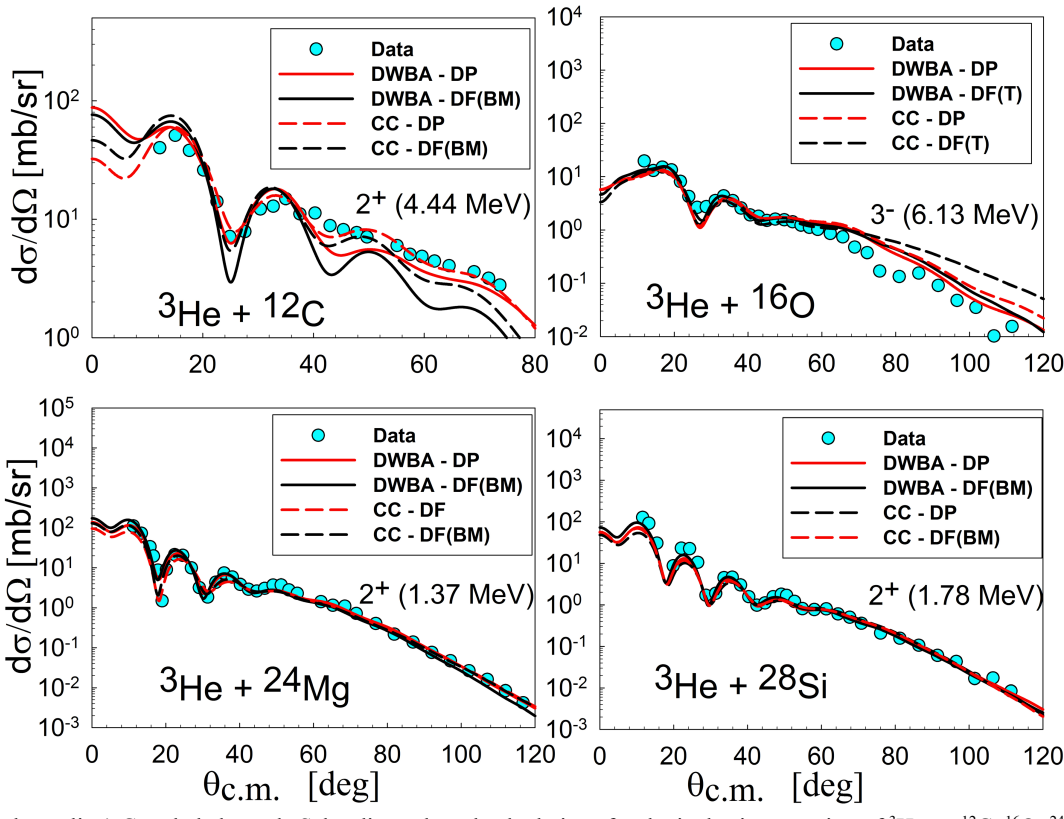


Fig. 13. (color online) Coupled channels Schrödinger-based calculations for the inelastic scattering of ³He on ¹²C, ¹⁶O, ²⁴Mg, and ²⁸Si at 60 MeV.

with the results of a previous study [19]. Burtebayev *et al.* considered the coupling of the elastic and inelastic scattering in the forward and reverse directions in the framework of the collective and microscopic models, respectively; nevertheless, the results were unsatisfactory (see Fig. 4 in [19]). The deformation decreased by 4.56% for the DP and increased by 1.63% for the DF potential. The DP produced a very consistent value of β .

For the 2⁺ state of ²⁴Mg, applying coupled channel calculations improved the results in the diffraction region for both DP and DF potentials. At large angles, the DWBA and CC calculations exhibited no significant difference. The present result exceeded the results obtained by Sadykov et al. (See Fig. 7 [24]) in the comparison. The authors utilized only the deformed real potential, which is a common approach in light particle scattering studies that enables them to compare their results with existing data. The present study provided evidence for the crucial role of imaginary part deformation in describing inelastic scattering. The coupling decreased the value of β . The DP produced $\beta = 0.436$, consistent with proton and electron scattering results. In contrast, the DF potential vielded $\beta = 0.562$, which aligns with findings from ³He scattering (see Table 5). Compared to the CC-DP results, the CC-DF results showed a marginal improvement.

For the 2^+ state of ${}^{28}{\rm Si}$, the implementation of coupled channel calculations demonstrated minimal enhancement in the accuracy of inelastic cross-section determinations. Consequently, coupled channel calculations had virtually no effect on the accuracy of inelastic cross-section predictions. The CC-DF calculations produced a β value of 0.322, which is consistent with proton and electron scattering experiment results. The CC-DP calculations yielded the lowest value of the deformation parameter. Similar to the case of ${}^{24}{\rm Mg}$, the CC-DF results showed only a marginal improvement over the CC-DP results, suggesting that the DF approach is not particularly advantageous for light targets.

Deformation parameters extracted from ³He scattering systematically exceeded those obtained from electron scattering, consistent with previous observations of projectile-dependent results [56]. This discrepancy arises because electron scattering interacts with protons solely via the Coulomb force, exclusively probing their charge distribution. In contrast, ³He scattering interacts with protons via both Coulomb and nuclear forces and with neutrons via the nuclear force, thereby exhibiting sensitivity to both neutron and proton distributions. The extracted deformation values could reflect dynamic deformation effects, where nuclear distortions emerged from the interplay between the internal structure of the target nucleus and incident projectile. Such dynamic deformation should fundamentally depend on both the nuclear structure and effective NN interactions during the scattering process. A comparison between the extracted deformation parameters and proton scattering results offers additional support for dynamical deformation effects, with the expectation that this effect will be more pronounced in ³He scattering because of its greater deformation magnitude.

IV. CONCLUSIONS

This study investigated the ³He elastic and inelastic scattering off ¹²C, ¹⁶O, ²⁴Mg, and ²⁸Si at 60 MeV using a DF approach. Optical potentials were calculated based on RMF-derived NN interactions R3Y(HS), R3Y(L1), R3Y(W), and R3Y(Z) for the real part. The results of the present study can be summarized as follows:

- 1. The regularization procedure maintained the characteristic behavior of NN interactions while reducing the potential well depth. The R3Y(Z) interaction was excluded from our analysis as a purely repulsive potential was deemed unphysical for ³He-nucleus scattering in this energy regime. Regularized potentials demonstrated improved agreement with experimental data. Comparative analysis revealed that the SWS imaginary potential provided results superior to those derived from folded potentials. In addition, the selection of imaginary potential affected the required normalization constant significantly.
- 2. The R3Y(HS) interaction successfully reproduced experimental scattering data with an optimal normalization constant $N \approx 1$ for ^{12}C and 0.9, 0.79 and 0.79 for ^{16}O , ^{24}Mg and ^{28}Si , respectively. In contrast, both R3Y(L1) and R3Y(W) interactions required significantly smaller normalization constants (N < 0.5), which produced unrealistically deep potentials that rendered them unsuitable for describing $^{3}\text{He-nucleus}$ scattering. We observed an inverse relationship between the normalization constant and target mass number, suggesting that the RMF-derived R3Y(HS) interaction demonstrated better performance for lighter nuclear systems.
- 3. Analysis of the inelastic scattering was conducted within the DWBA framework, employing two distinct approaches for transition potentials: a phenomenological DP and a microscopic DF potential. The DP approach yielded a larger potential depth for the 2⁺ excited state of ¹²C than the DF method. Although both models successfully reproduced small-angle scattering cross-sections, their accuracy diminished at larger angles, with the DP model demonstrating a better performance in this regime. For the ¹⁶O's 3⁻ state, the DF approach based on BM collective models required an anomalously large deformation parameter ($\beta_3 > 0.5$). A better agreement with experimental data was achieved using a Tassie-type transition density, which provided more realistic nuclear deformation characteristics. For the 2⁺ states of ²⁴Mg and ²⁸Si, both DP and DF approaches incorporating BM transition

densities produced comparable and satisfactory results across the measured angular range.

4. The CC method was applied to analyze both elastic and inelastic scattering processes, demonstrating varying degrees of success across different nuclear systems. For elastic scattering, the CC calculations showed excellent agreement with experimental data in the angular range of 10°–100°, particularly for the ¹²C nucleus, which accurately reproduced the characteristic oscillatory pattern observed between 80°–120°. An analysis of the effects of coupling various transition potentials on elastic scattering revealed that CC-DP consistently outperformed the DF potential approach with BM densities (CC-DF), with the latter exhibiting phase discrepancies beyond 120° that limited its effectiveness for backward-

angle scattering. In the analysis of inelastic scattering, the CC method proved effective for the ¹²C nucleus, significantly improving the agreement with experimental data across both forward and backward angles for both transition potential formulations, thereby suggesting strong coupling between nuclear states in this system. Further, the method provided accurate descriptions of the 3⁻ state in ¹⁶O for scattering angles up to 50°; however, its effectiveness diminished at larger angles regardless of the potential used. The results were more varied for the 2⁺ states of heavier nuclei: the ²⁴Mg case showed noticeable improvement in the diffraction region. Meanwhile, the ²⁸Si system exhibited only minimal enhancement in cross-section determination, indicating weaker coupling effects in these heavier nuclei.

References

- [1] M. E. Brandan and G. R. Satchler, Phys. Rep. **285**, 143 (1997)
- [2] D. T. Khoa and G. Satchler, Nucl. Phys. A 668, 3 (2000)
- [3] L. C. Chamon, B. V. Carlson, L. R. Gasques *et al.*, Phys. Rev. C. 66(1), 014610 (2002)
- [4] V. Lukyanov, E. Zemlyanaya, and K. Lukyanov, Phys. At. Nucl. 69, 240 (2006)
- [5] Z. M. Mahmoud, Phys. Rev. C **105**(4), 044609 (2022)
- [6] F. Pakdel, A. Rajabi, and L. Nickhah, Pramana 87, 1 (2016)
- [7] M. Aygun, Pramana **96**(4), 209 (2022)
- [8] B. Sahu, S. Singh, M. Bhuyan *et al.*, Pramana **82**, 637 (2014)
- [9] C. Horowitz and B. D. Serot, Nucl. Phys. A **368**, 503 (1981)
- [10] P. -G. Reinhard, Rep. Prog. Phys. **52**, 439 (1989)
- [11] B. Singh, M. Bhuyan, S. Patra et al., J. Phys. G: Nucl. Part. Phys. 39(2), 025101 (2012)
- [12] W. Yahya and B. Falaye, Nucl. Phys. A **1015**, 122311 (2021)
- [13] M. Aygun, Z. Aygun, and N. Karaali, Acta Physica Polonica B **54**, 5-A1 (2023)
- [14] N. Burtebayev, A. Duisebayev, B. Duisebayev *et al.*, Acta Physica Polonica B **47**(8), 2017 (2016)
- [15] D. Janseitov, S. Lukyanov, K. Mendibayev et al., International Journal of Modern Physics E 27(10), 1850089 (2018)
- [16] S. Khallaf, A. Nossair, A. Ebrahim *et al.*, Nucl. Phys. A 714, 412 (2003)
- [17] A. Denikin, S. Lukyanov, N. Skobelev *et al.*, Phys. Part. Nucl. Lett. 12, 703 (2015)
- [18] S. Khallaf, A. Amry, and S. Mokhtar, Phys. Rev. C **56**(4), 2093 (1997)
- [19] N. Burtebayev, A. Duysebayev, B. Duysebayev et al., International Journal of Modern Physics E. 26(04), 1750018 (2017)
- [20] C.-T. Liang, X.-H. Li, and C.-H. Cai, J. Phys. G: Nucl. Part. Phys. 36, 085104 (2009)
- [21] M. Lantz, Investigations of Reaction Cross Sections for Protons and ³He, Ph. D. Thesis (Uppsala: Acta Universitatis Upsaliensis, 2005)
- [22] S. Hamada, Y. Hirabayashi, N. Burtebayev et al., Phys.

- Rev. C 87(2), 024311 (2013)
- [23] S. Adachi, T. Kawabata, K. Minomo et al., Phys. Rev. C 97, 014601 (2018)
- [24] B. Sadykov, T. Zholdybayev, N. Burtebayev *et al.*, Eur. Phys. J. A 57(4), 130 (2021)
- [25] B. Sadykov, M. Nassurlla, B. Duisebayev *et al.*, Вестник. Серия Физическая (ВКФ) **79**, 17 (2021)
- [26] D. T. Khoa, W. Von Oertzen, and H. Bohlen, Phys. Rev. C. 49(3), 1652 (1994)
- [27] D. T. Khoa and O. Knyazkov, Zeitschrift für Physik A Atomic Nuclei 328, 67 (1987)
- [28] D. T. Khoa and O. Knyaz'kov, Sov. J. Nucl. Phys. 47, 5 (1988)
- [29] R. Brockmann, Phys. Rev. C. 18(3), 1510 (1978)
- [30] L. Miller and A. E. Green, Phys. Rev. C. **5**(1), 241 (1972)
- [31] R. Brockmann and W. Weise, Phys. Rev. C. **16**(3), 1282 (1977)
- [32] K. Lukyanov, V. Lukyanov, E. Zemlyanaya *et al.*, Eur. Phys. J. A **33**, 389 (2007)
- [33] M. Avrigeanu, G. Anagnostatos, A. Antonov *et al.*, International Journal of Modern Physics E 11, 249 (2002)
- [34] R. Machleidt, The meson theory of nuclear forces and nuclear structure, in Advances in nuclear physics, Vol. 19 (Springer, 1989)
- [35] V. Stoks, R. Klomp, C. Terheggen et al., Phys. Rev. C. 49(6), 2950 (1994)
- [36] M. Avrigeanu, A. Antonov, H. Lenske *et al.*, Nucl. Phys. A 693, 616 (2001)
- [37] H. Chandra and G. Sauer, Phys. Rev. C. **13**(1), 245 (1976)
- [38] V. Choudhary, W. Horiuchi, M. Kimura *et al.*, Phys. Rev. C 102(3), 034619 (2020)
- [39] K. Kuterbekov, A. Kabyshev, A. Azhibekov *et al. Investigation of elastic scattering of ³He on ²⁸Si nucleus in energy range 8–217 MeV.* in EXOTIC NUCLEI: EXON-2016 Proceedings of International Symposium (World Scientific, 2017)
- [40] Q.-B. Shen, D.-Ch. Feng, and Y.-Zh. Zhuo, Phys. Rev. C 43(6), 2773 (1991)
- [41] M. Karakoc and I. Boztosun, Phys. Rev. C **73**(4), 047601
- [42] C. R. Ottermann, G. Köbschall, K. Maurer et al., Nucl. Phys. A 436, 688 (1985)

- [43] K. O. Behairy, Z. M. Mahmoud, and M. Anwar, Nucl. Phys. A 957, 332 (2017)
- [44] D. Horen, G. Satchler, S. Fayans et al., Nucl. Phys. A 600, 193 (1996)
- [45] A. N. Bohr and B. R. Mottelson, *Nuclear Structure (in 2 volumes)* (World Scientific Publishing Company, 1998)
- [46] M. Vineyard, J. Cook, and K. Kemper, Nucl. Phys. A 405, 429 (1983)
- [47] J. Raynal, CEA Saclay report CEA-N-2772 (1994)
- [48] M. Karakoç, Comput. Phys. Commun. 284, 108613 (2023)
- [49] M. Yasue, T. Tanabe, F. Soga et al., Nucl. Phys. A 394, 29 (1983)
- [50] Y. Horikawa, Y. Torizuka, A. Nakada et al., Phys. Lett. B

- **36**, 9 (1971)
- [51] H. Hans, *Nuclear Physics: experimental and theoretical*, (New Age International, 2008), p. 453
- [52] L. Tassie, Australian Journal of physics 9, 407 (1956)
- [53] A. Kobos, B. Brown, R. Lindsay et al., Nucl. Phys. A 425, 205 (1984)
- [54] N. Keeley, K. Kemper, and K. Rusek, Eur. Phys. J. A 50, 1 (2014)
- [55] V. Lapoux, N. Alamanos, F. Auger et al., Phys. Rev. C 66(3), 034608 (2002)
- [56] W. Vermeer, M. Esat, J. Kuehner *et al.*, Phys. Lett. B 122, 23 (1983)